Peer-reviewed version available at European Journal of Remote Sensing 2019, 52, 17-31; doi:10.1080/22797254.2019.1642143

Article

Aerial Multispectral Imagery for Plant Disease Detection; Radiometric Calibration Necessity Assessment

Hossein Pourazar [1], Farhad Samadzadegan [1] and Farzaneh Dadrass Javan [1,*]

[1] School of Surveying and Geospatial Engineering, College of Engineering, University of Tehran, Iran; (h.pourazar, samadz, fdadrasjavan,) @ut.ac.ir

* Correspondence: fdadrasjavan@ut.ac.ir; Tel.: +98-21-88008841

Abstract: In recent years, using multispectral cameras on UAVs has provided an opportunity to capture separate bands that offer the extraction of spectral features used for early detection of diseased plants. One of the main steps in disease detection is radiometric calibration that converts digital numbers to reflectance values commonly using white reference panels. This paper focused on the necessity of radiometric calibration to distinguish disease trees in orchards based on aerial multi-spectral images. For this purpose, two study sites with various climate conditions and tree species as well as different disease types were selected where multispectral images were taken using a multirotor UAV. The impact of radiometric correction on plant disease detection was assessed in two ways: 1) comparison of separability between the healthy and diseased classes using T-test and entropy distances; 2) radiometric calibration effect on the accuracy of classification. The experimental result showed the insignificant effect of radiometric calibration on separability criteria. Furthermore, based on T-test and entropy distances criteria, NIR and R spectral features made highest distances between healthy and Greening infected citrus trees, respectively, at the first study site while NDRE and BNDVI spectral features made highest distances between healthy and peach leaf curl infected trees, respectively, at the other study site. In the second strategy, the experimental result showed that radiometric calibration had no effect on the accuracy of classification. As a result, the overall accuracy and kappa values for both un-calibrated and calibrated orthomosaic classifications of the citrus orchard were 96.6% and 0.94%, respectively, using five spectral bands as well as DVI, NDRE, NDVI and GNDVI vegetation indices using a random forest classifier. The experimental results were also similar at the other study site. Therefore, the overall accuracy and kappa values for both the un-calibrated and calibrated orthomosaic classifications were 96.1%, 0.92, respectively, using five spectral bands as well as NDRE, BNDVI, GNDVI, DVI, and NDVI vegetation indices.

Keywords: multispectral; radiometric calibration; classification; plant disease; Aerial imagery

1. Introduction

In recent years, the prediction of effective challenges on the crop yield such as climate change effects, diseases, and pests has become a critical issue in food managing strategies [1]. Furthermore, because of the population increase and instability of agricultural production due to climate variability, some methods and techniques have been developed for monitoring the condition of plants as well as the quality and quantity of agricultural products.

Apparently, the inspection procedure for the early detection of the bacteria presence is extremely time consuming. Therefore, it is necessary to find a detection process which will be faster than the field inspection by experts [2]. The limitations of direct field inspection methods have led researchers

Peer-reviewed version available at European Journal of Remote Sensing 2019, 52, 17-31; doi:10.1080/22797254.2019.1642143

to investigate remote sensing data to quickly and inexpensively obtain plant health information. Non-destructive remote sensing data permits measurement of biophysical and biochemical parameters of plants for nondestructive monitoring of plant growth and health [3-5]. These methods are based on the optical properties of plants and can be used for identifying nutrient deficiencies, plants diseases, minimum water and excess water, insect damage, weeds, etc. [3, 6-8]. Combination of plant knowledge and remote sensing data can provide information for plant management and even initial advices about plant stress to prevent the spread of disease or pest infestation by adopting appropriate reactions in the early stages of stress.

In recent years, numerous remote sensing applications have been studied for monitoring the health of plants through using satellite [9, 10], airborne [10-14] and ground-based [15-20] remote sensed data. Multispectral images as well as related vegetation indices status ([21]; [9]; [12, 13]) and hyperspectral images ([22]; [10], [14]) are used in the airborne and space-borne remote sensing to study the health of plants. Ground-based remote sensing data is usually used to identify the best wavelengths along with optimum vegetation indices related to the effect of pest, disease and nutrient deficiency in plants with high correlation ([15] [18]. [19] [20]). More recently, in the remote sensing application, manned airborne vehicles are replaced with unmanned aerial vehicles (UAVs), which can be deployed quickly and repeatedly, and also have flexible flying height and timing of missions as well as high-resolution imagery [23].

One of the main steps of image post-processing in remote sensing applications is the extraction of absolute reflectance measurements from the data in the radiometric calibration process [24]. It should be noted that the necessity of camera calibration is an open question. Therefore, this study investigated the potential of UAV based multispectral imagery in plant disease detection and especially concentrated on the necessity of radiometric calibration.

The first study area was a citrus orchard with the Greening disease. The citrus Greening disease has become one of the greatest challenges for citrus growers across the world [25]. Citrus Greening, transmitted by grafting from citrus to citrus, can severely weaken citrus trees, causing reductions in fruit yield and quality. A sample of Greening symptoms on citrus tree leaves is presented in

(a) (b)

Figure 1(a).

The other study area is a peach orchard with the peach leaf curl (PLC) disease. The PLC fungal disease is one of the most common diseases of peach trees in the north of Iran that mostly affects peaches leaves and nectarines. PLC is caused by the ascomycetous fungus Taphrina deformans and causes parts of individual peach leaves to become curled and pale green or reddish in color (

(a) (b)

Figure 1(b)) [26]. Taphrina deformans primarily affects a foliage, but may also affect fruits and young twigs [27].

Peer-reviewed version available at European Journal of Remote Sensing 2019, 52, 17-31; doi:10.1080/22797254.2019.1642143

(a) (b)

Figure 1. (a) Greening symptoms on citrus tree leaves; (b) the PLC sample

1.1. Related Works

The fast technology development in UAV systems and the advent of small scale UAVs, which can carry small visible and multispectral sensors, provide the opportunity to capture high spatial and spectral resolution data, especially for agricultural application. In multispectral images, a variety of spectral bands offer the extraction of vegetation indices to distinguish diseased and healthy plants [23, 28-33].

To investigate the potential of the nutrient deficiency using UAV based multispectral images, Agüera et al. compared the correlation between the calculated NDVI from UAV based multispectral images and the ground-based multispectral radiometer with the nitrogen status in a sunflower field [28]. Results proved a higher correlation coefficient (R=0.80) using the UAV platform than a ground-based measurement (R=0.71). In another study, Garcia-Ruiz et al. investigated the capability of UAV-based multispectral images using for citrus greening detection in comparison with similar images captured based on piloted aircraft [29]. They achieved classification accuracy of 67–85% and 61–74% based on UAV-based and aircraft-based datasets, respectively, using six spectral bands as well as NDVI, GNDVI, SAVI, NIR–R, R/NIR, green(G)/R and NIR/R vegetation indices. To detect the citrus Greening disease, Sarkar et al. also presented an UAS sensor set including an onboard active spectrally selective light source and an RGB-D sensor that measures distance and reflectance of rotated polarized light [32]. They used a liner SVM classifier and reported 93% classification accuracy.

De Castro et al. evaluated the spatial and spectral of multispectral requirements of images for quick and accurate detection of laurel wilt (LW) disease in an avocado field, considering the change in the flight altitudes and spectral sensors. Results demonstrated that most effective spectral wavelengths were 580–10 nm, 650–10 nm, 740–10 nm, 750–10 nm, 760–10 nm and 850–40 nm with 15.3 cm spatial resolution and the optimum vegetation indices were TCARI760–650, GNDVI, NIR/G, Redge/G and VIGreen using Redge or NIR bands [31].

Albetis et al. evaluated the capability of spectral features computed from the UAV multispectral imagery including spectral bands, vegetation indices and biophysical parameters for discriminating the Flavescence dorééesymptoms disease in red and white cultivars from healthy vine vegetation. Results presented best with red cultivars, but were not acceptable for white cultivars [33].

The radiometric calibration of the UAV based multispectral images is one of the main steps of image processing in remote sensing applications [24]. For the purpose, especially in UAV based remote sensing applications, usually an image-based empirical approach, called empirical lines based methods, is used [34]. This technique is based on the assumption of an empirical relationship between the image DNs and the at-surface reflectance which is made as a field measure of the appropriate Targets[35].

Kelcey and Lucieer for radiometric calibration of UAV based multispectral images of mini-MCA camera, used three radiometric targets made of a plywood and backing with a white tyvac, grey fabric and black fabric covers. The targets' at-surface reflectance were measured by an ASD HandHeld 2 Portable Spectrometer [24]. In study, two black and white calibration targets with 3% and 82% reflectance, respectively, were used during flight for radiometric correction in empirical line calibration method which was carried out in ENVI software [31].

On the other hand, along with a UAV based multispectral cameras, a white calibration panel is usually provided for radiometric calibration. Miura and Huete evaluated three white calibration panel based radiometric calibration methods in the hypersonic airborne data, called "reflectance mode", "linear interpolation" and "continuous panel" [36]. These methods used white calibration panel to convert DN to at-surface reflectance. Clemens modified the "reflectance mode" method from

Peer-reviewed version available at European Journal of Remote Sensing 2019, 52, 17-31; doi:10.1080/22797254.2019.1642143

Miura and Huete (2009) to reduce the reflectance value conversion bias [37]. In this study, an average of the pre- and post-flight panel readings in the reflectance conversion is used which assumed a linearity due to the short time of flight. Garcia-Ruiz et al. used white board for radiometric calibration of the UAV-based images to ensure that 100% reflectance corresponding with a digital number of 255 [29]. Albetis et al. also used the calibrated ground panel, before and after the flight, to convert the DN to at-surface reflectance in each band [33].

As shown in the literature, radiometric calibration is considered as the main step in UAV based plant disease detection, and measurements of reference targets are implemented in empirical line based methods by default, while the efficacy and necessity of this step is unclear. Therefore, the efficacy and necessity of the radiometric calibration step in plant disease detection using UAV based multispectral images were investigated in this study.

2. Materials and Methods

2.1. Study Area and Imaging System

Two different agricultural fields located in the north and south of Iran were selected as the study area. The first one, a citrus orchard outbreak with Greening disease, is located in Fasa County, Fars Province, Iran (

(a) (b)

Figure 2-a). The second field is located in Neka City, Mazandaran Province, Iran, which is a peach orchard affected by the PLC disease (

(a) (b)

Figure 2-b).

Preprints (www.preprints.org) | NOT PEER-REVIEWED | Posted: 13 February 2019 doi:10.20944/preprints201902.0111.v1

Peer-reviewed version available at European Journal of Remote Sensing 2019, 52, 17-31; doi:10.1080/22797254.2019.1642143

Figure 2. a) First data set; Citrus orchard in Fasa, b) Second data set; Peach orchard in Neka

A small multirotor platform that is equipped with Micasense RedEdge multispectral camera, which is especially designed for agriculture applications, is selected for imaging of both test fields. A summary on specifications of both platform and imaging system is presented in **Table 1**.

Table 1. Platform and imaging system specifications

Platform		**Multispectral sensor**	
Platform Type	Hexa-copter	Spectral bands	Blue- Green-Red-RE-NIR
Flight Duration	40 min	size	12.1 x 6.6 x 4.6 cm
Max Flight Altitude	200m AGL	weight	150g
Max takeoff weight	6 kg	Field of view	47.2 º HFOV
Dimension	1.2 m	Focal length	5.5 mm
			

To achieve reliable and efficient multispectral images, accurate flight planning is needed in order to achieve optimum image resolution and accuracy at the best flight time and cost. Some details on the flight planning parameters in the both study areas are presented in Table 2.

Table 2. The flight planning parameters of the study sites

	Fasa	**Neka**
Flight Altitude (m)	25	10
Area (m²)	16.2e+03	3.44e+03
Flight Time (min)	~17	~15
Ground Resolution (mm/pix)	12.7	6.43
Number of Images	494	760
No of Strips	20	17
Footprint (m2)	16.25x12.45	8.23x6.17
Overlap	75%	80 %
Sidelap	75%	70 %

Disease and healthy trees as ground truth were selected by the experts' visual inspection and labeled using special targets (Figure 5) before image acquisition to train and test the classifier. Therefore, 15 citrus Greening infected and 10 healthy trees at the Fasa study area as well as 20 PLC infected and 12 healthy trees at the other study area were selected as ground truth data.

Peer-reviewed version available at European Journal of Remote Sensing 2019, 52, 17-31; doi:10.1080/22797254.2019.1642143

161

162 *2.2. Processing Methodology*

163 Figure 3 summarizes the workflow of proposed methodology for plants disease detection based
164 on multispectral imagery and assessment of radiometric calibration evaluation necessity.

165 Acquired multilens images were registered band-to-band in the first step and then aligned in
166 the bundle adjustment process. Regarding the image acquisition under different illumination
167 conditions, the normalization of image blocks is necessary in order to produce homogeneous block
168 which is done based on radiometric block adjustment. Finally, Band registered aligned Images
169 stitched together to produce ortho-music. In [24, 29, 31, 33, 38, 39], commonly radiometric calibration
170 is done as the main step that convert DN to reflectance. In order to evaluate the radiometric
171 calibration necessity of multispectral images and to inspect its effects on the quality of final results,
172 classification process is performed both on DN (Strategy II) and reflections based data (Strategy I)
173 and results were evaluated and discussed. The classification process consisted of three main steps:
174 feature space generation; train classifier and performs classification to generate disease map.

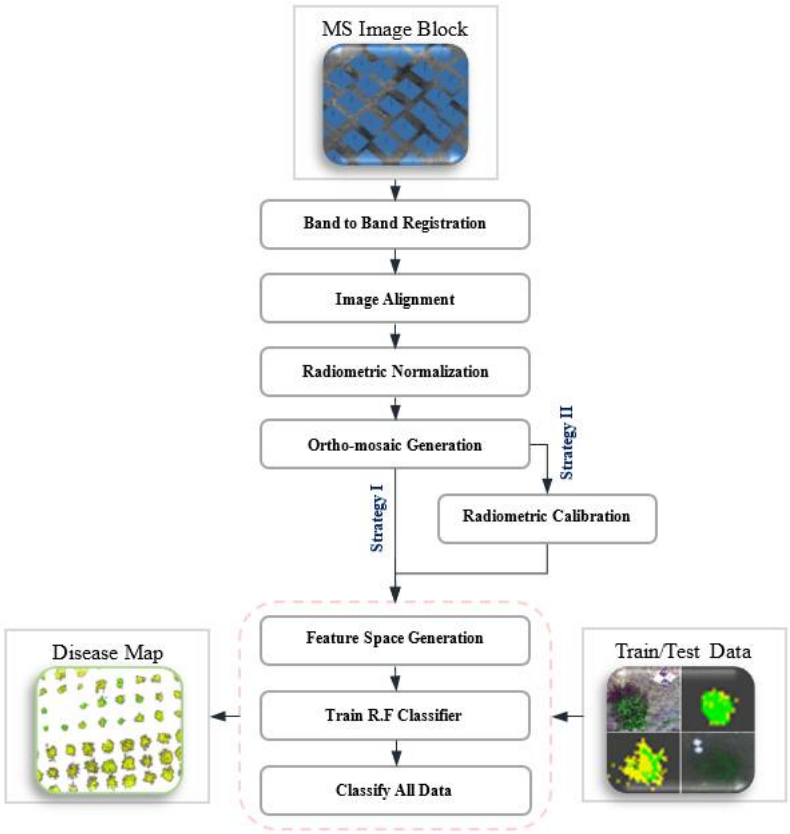

175

176 **Figure 3.** Data Processing Flow Diagram. Strategy I: Processing without Radiometric Calibration;
177 Strategy-II: Processing based on reflectance orthomusaic by perform Radiometric Calibrated

178

Preprints (www.preprints.org) | NOT PEER-REVIEWED | Posted: 13 February 2019 doi:10.20944/preprints201902.0111.v1

Peer-reviewed version available at European Journal of Remote Sensing 2019, 52, 17-31; doi:10.1080/22797254.2019.1642143

179 2.2.1. *Band-to-band Registration*

180 Recent developed UAV based multispectral cameras are usually composed of multilens
181 structure (Figure 4). Due to the low altitude of flight in small UAV, Band miss-registration of
182 multispectral images acquired by multilenses cameras is a great challenge [40]. In this study, SIFT[1]
183 algorithm is applied to extract corresponding features from images. It is well suited for the feature
184 detection and description because it is able to handle the special characteristics of the input data such
185 as low image contrast as well as rotation, translation and scale differences [41]. After extraction of
186 feature points using SIFT algorithm, the matching process can be done by comparing the minimum
187 Euclidean distance between the extracted feature vectors. With the matched features, the
188 mathematical relationship between the two images will be computable. Finally, the images were
189 registered and resampled based on the projection transformation [42].

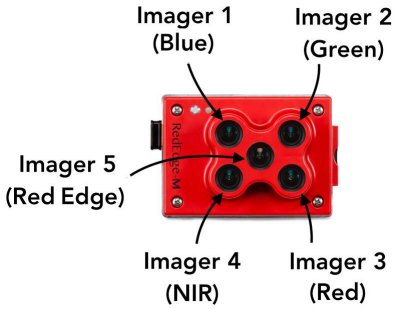

190

191 **Figure 4:** The MicaSense RedEdge as an advanced multilens and multispectral camera specially
192 designed for small UAVs.

193 2.2.2. Image Alignment

194 Image alignment provides interior and exterior orientation parameters in the bundle adjustment
195 process that use tie points in overlapping images [43]. Tie points could be extracted by the SIFT
196 algorithm. The SIFT algorithm detects features and matches corresponding features in overlapping
197 images; moreover, outliers and improper matches are eliminated simultaneously [44]. Thus, a sparse
198 point cloud will be an output of the bundle adjustment [39]. This process is carried out effectively
199 due to consideration of sufficient overlap and side laps of images during a flight mission.
200

201 2.2.3. Radiometric Normalization

202 Regarding the image acquisition under different illumination conditions, the radiometric
203 normalization of image blocks is necessary in order to produce homogeneous orthomusaic.
204 According to Gehrke and Beshah [45], the radiometric normalization parameters for all images in the
205 block are computed in the least squares adjustment using radiometric tie points. The main
206 observation equation for each radiometric tie point (extracted geometric tie points in image alignment
207 step) between two images can be expressed as Equation (1):

$$0 = \{c_{xy} DN_{xy} + b_{xy}\}_{\mathrm{Im}gA} - \{c_{xy} DN_{xy} + b_{xy}\}_{\mathrm{Im}gB} \quad (1)$$

208 where c_{xy} and b_{xy} are the normalization parameters. For the radiometric control points on the
209 reference image, Equation (1) is rewritten as Equation (2):

$$\{DN_{xy}\}_{\mathrm{Re}f\,\mathrm{Im}g} = \{c_{xy} DN_{xy} + b_{xy}\}_{Adj\,\mathrm{Im}gA} \quad (2)$$

210 Radiometric control points were applied to define the 'radiometric datum' [45].

[1] Scale Invariant Feature Transform

Peer-reviewed version available at European Journal of Remote Sensing 2019, 52, 17-31; doi:10.1080/22797254.2019.1642143

2.2.4. Orthomusaic Generation

Because of the small footprint of each image, the acquired images were geometrically corrected and merged to produce a seamless orthomusaic of the whole area.

In UAV imagery based applications, dense point cloud extraction based on the aligned images is a main step commonly [30, 39, 46, 47]. Finally, orthomusaic was generated based on aligned images and dense point cloud; Thus, the topographic relief of trees was considered there. However, in this study, an orthomusaic without trees topographic relief consideration satisfied our goals. Therefore, orthomusaic is generated based on aligned images and one coarse DSM producing from the sparse point cloud.

2.2.5. Radiometric Calibration

One of the main steps in image processing for remote sensing applications is the radiometric calibration process where the absolute reflectance measurements from the DN data is extracted [24]. Acquired images could be calibrated using radiometric reference images that captured from a calibrated reflectance panel before and after each flight [37].

In this study, "reflectance mode" method is applied for radiometric calibration based on Clemens [37]. In the Clemens method, an average of the pre- and post-flight panel measurements is used in the reflectance conversion. Equation (3) presents the basis of the reflectance factor calculation in the reflectance mode method.

$$R_T = \frac{DN_T}{DN_R} R_R \quad (3)$$

where DN_T is digital numbers of the target; DN_R is the average of the pre- and post-flight in reference in images; and R_R is the reflectance factor of the white panel which will determine R_T, the reflectance factor of the unknown surface.

2.2.6. Feature Space Generation

One of the simplest techniques to map the vegetation is to use vegetation indices that are easily calculable and understandable [48]. Numerous vegetation indices are calculated as the difference or ratio of two or several bands in the wide range of the spectrum (e.g., NDVI, RVI, etc.). They constitute the simple and straight method to extract highly correlated information to biophysical parameters of plants from remotely sensed data. After extraction of ortho images, spectral features including five spectral bands and 12 vegetation indices were extracted to be applied in the classification (Table 3). In Table 3, B, G, R, RE and NIR are the blue, green, red, red edge, and near infra-red bands of the multispectral images, respectively.

After calculating the spectral features, the most suitable features that discriminated between the healthy and unhealthy trees were selected in this study. Decreasing the number of features, increases the generalization capability and reduces the computational complexity of the classification algorithm [49]. The T-test and entropy distances measure the separability between two classes and can be used as criteria to evaluate the efficacy of each feature for discriminating between healthy and unhealthy trees classes.

Table 3. Applied vegetation indices

Index	Formula	Reference
Ratio Vegetation Index	$RVI = \frac{NIR}{R}$	[50]
Normalized Difference Vegetation Index	$NDVI = \frac{NIR - R}{NIR + R}$	[17, 51]
Green Normalized Difference Vegetation Index	$GNDVI = \frac{NIR - G}{NIR + G}$	[52]
Green Ratio Vegetation Index	$GRVI = \frac{NIR}{G}$	[53]
Blue Normalized Difference Vegetation Index	$BNDVI = \frac{NIR - B}{NIR + B}$	[54]
Red Edge Normalized Difference Vegetation Index	$NDRE = \frac{NIR - RE}{NIR + RE}$	[17, 55]
Infrared Percentage Vegetation Index	$IPVI = \frac{NIR}{NIR + R}$	[56]
Structure Insensitive Pigment Index	$SIPI = \frac{NIR - B}{NIR - R}$	[17, 57]
Optimized Soil-Adjusted Vegetation Index	OSAVI = (NIR-R)/(NIR+R+0.16)	[9]
Chlorophyll Index	$CI = \frac{NIR}{G} - 1$	[58, 59]
Difference Vegetation Index	DVI = NIR-R	[60]
Greenness Index	$GI = \frac{G}{R}$	[61]

2.2.7. Classification

After feature space generation, the final step towards health map generation is the classification of images based on selected training data. For this purpose, a random forest classifier, developed by Breiman [62], is used due to its simplicity and high performance [63, 64]. Random forests non-parametric classifier is an ensemble-based machine-learning algorithm that engages the multiple decision tree classifiers in a voting strategy to provide the final prediction. It consists of several decision tree classifiers that build using a bootstrap sample of the data with a random variable set at each node to split on.

Implementation of random forest classifiers requires a few parameters, including the number of trees and the number of randomly selected predictor variables [65]. So random forest offer less complex computations and running time, as well as high performances in computer vision domain especially [66]. In this study, we used a random forest classifier consisting of 100 decision trees.

The final accuracy in detection of the diseased and healthy trees is tested by calculating error matrices of the test data (references). The error matrix presents the error of omission, error of commission, overall accuracy and kappa (κ) values (references).

3. Experiments and Results

In this study, we evaluated the impact of radiometric calibration on UAV based multispectral plant disease detection using the two datasets with different disease and environmental conditions. For this, 557 images from the Fasa test area and 683 images from the Neka test area were captured based on the flight plan.

3.1. Band-to-band Registration

The first processing step is spectral bands registration of images. Due to the multilenses structure of multispectral camera, a considerable geometric displacement between images captured by lenses appeared. To remove the displacements, the red band was selected as the master and the rest were considered as slaves which should be registered to the master. The band registration of all the images were conducted based on the proposed strategy and the RMSE value of 0.4 pixels was available based

Peer-reviewed version available at European Journal of Remote Sensing 2019, 52, 17-31; doi:10.1080/22797254.2019.1642143

on the target measurement. Figure 5 shows two false color images of the same scene: original image and band registered image as a sample.

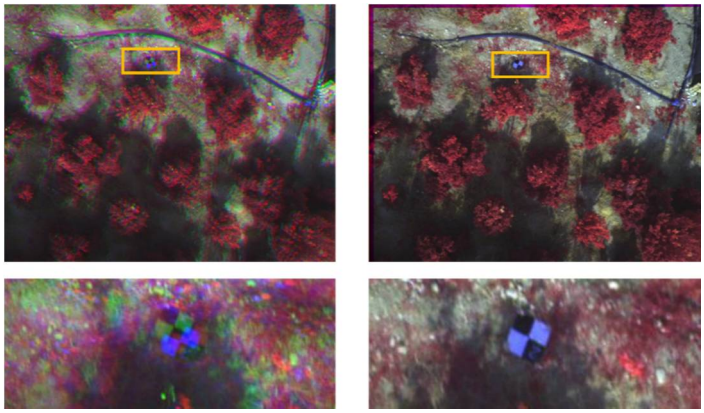

Figure 5. Spectral bands registration of Micasense RedEdge camera images; Right: uncorrected, Left: Corrected.

3.2. Image Alignment and Seamless Orthomosaic Generation

After band registration step, a seamless orthomosaic of the whole area covering in the imagery step should be generated with five spectral bands. For this purpose, multispectral images must be aligned. In this step, geometric tie points were extracted, and image interior and exterior parameters were estimated. Table 4 presents the summary of the block adjustment parameters.

Table 4. Summary of the block adjustment parameters

	Fasa Site	Neka Site
Number of images	1470	3800
Tie points	2,529,731	2,534,329
RMS reprojection error	(0.66246 pix)	(0.85034 pix)
Max reprojection error	(31.9115 pix)	(27.3773 pix)

Based on the aligned band registered images, a dense point cloud was produced and used in orthomosaics generation. The specification of the dense point cloud and orthomosaics are presented in Table 5.

Table 5. Specification of dense point clouds and orthomosaics

		Fasa Site	Neka Site
Orthomosaic	Resolution(cm/pix)	1.27	0.643
	Size (pixel)	12713x15413	7485x15283
Dense Point Cloud	Size (point)	26909315	25386097

The generated orthomosaics are depicted in Figure 6.

Peer-reviewed version available at European Journal of Remote Sensing 2019, 52, 17-31; doi:10.1080/22797254.2019.1642143

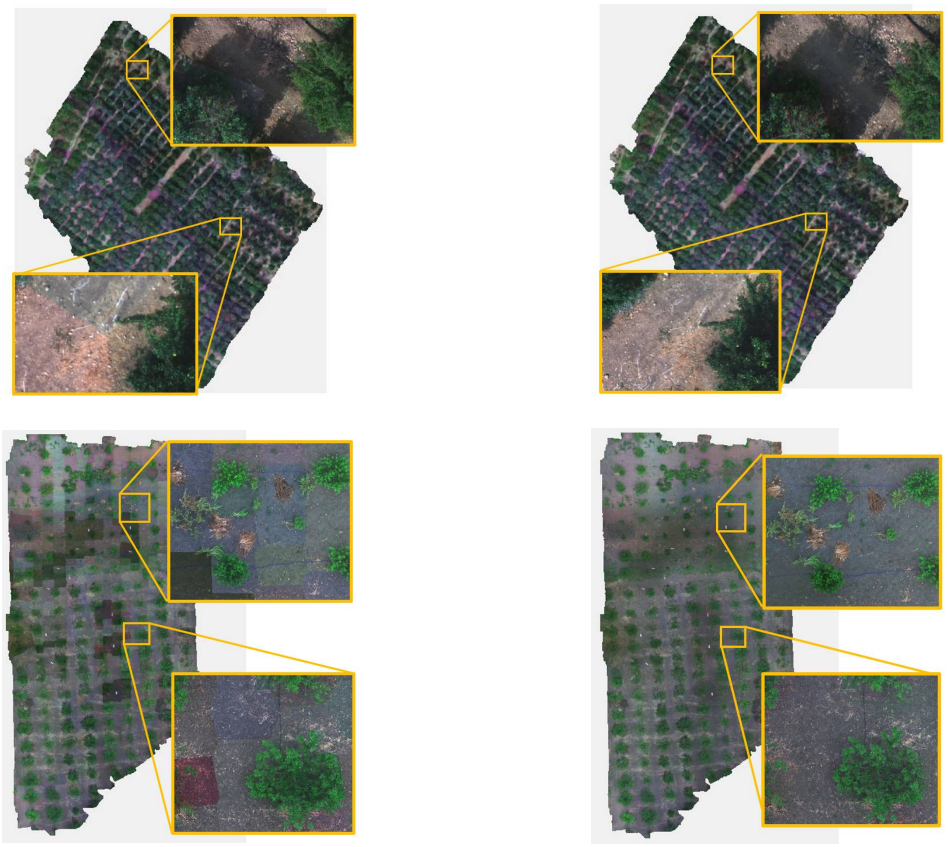

Figure 6: Left up: Fasa study site orthomosaic without radiometric normalization, Right Up: Fasa study site orthomosaic with radiometric normalization. Left down: Neka study site orthomosaic without radiometric normalization, Right down: Neka study site orthomosaic with radiometric normalization.

As is depicted in Figure 6, a seamless orthomosaics was generated after radiometric normalization which was prepared for the feature extraction and classification processing step.

3.3. Radiometric Calibration

For the radiometric calibration process, reference images of a white panel were captured immediately before and after each flight. A sample image acquired from the calibrated reflectance panel is presented in Figure 7.

Figure 7. Left: reflectance panel image acquisition, right: Red edge band captured from reflectance panel.

Peer-reviewed version available at European Journal of Remote Sensing 2019, 52, 17-31; doi:10.1080/22797254.2019.1642143

Maximum DNs in the images captured from the white panel, before and after the flight (BF and AF, respectively), are listed in Table 6 for the both study data sets.

Table 6. The maximum DN of the white panel in the five spectral bands

	Fasa Site		Neka Site	
Spectral Band	BF	AF	BF	AF
Blue	57488	55424	52000	32320
Green	59152	58304	47744	34480
Red	54480	53248	42816	28128
NIR	58048	55280	44208	29696
RedEdge	59472	53696	44624	26784

DNs values are related with at-sensor radiance directly; Thus, Table 6 shows the decrease in at-sensor radiance during the both flights. The rate of this reduction was much higher at the Neka site, which indicated a significant change in illumination conditions during that flight. The mean DN values of BF and AF were used in Equation (3) to calculate the reflectance-based values and new orthomosaics were generated based on these new values for each study data.

3.4. Spectral Feature Analysis

Feature space in our study includes five spectral bands (Blue, Green, Red, RE and NIR) and 12 vegetation indices (RVI, NDVI, GNDVI, GRVI, BNDVI, NDRE, IPVI, SIPI, OSAVI, CI, DVI and GI).

In order to investigate the necessity of sensor calibration for vegetation disease detection, separability between healthy and un-healthy tree classes, related features were investigated using T-test and entropy criteria using ground truth data collected from the calibrated and un-calibrated data for the both study areas. The experimental results are presented in Figure 8.

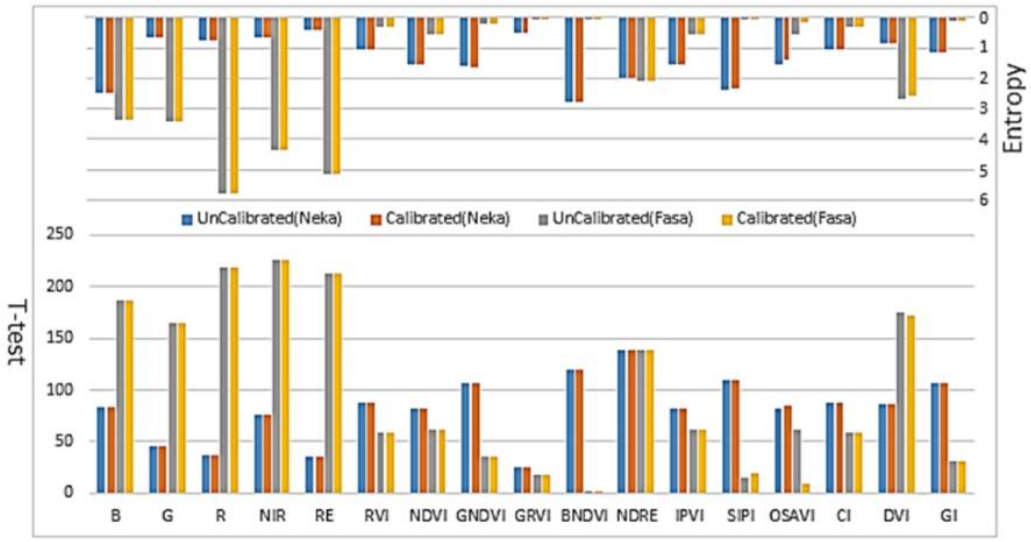

Figure 8: The distance between healthy and un-healthy classes based on T-test and entropy criteria in ground truth data collected from calibrated and un-calibrated based orthomosaics

Considering the achieved values presented in Figure 8, it can be concluded that the camera calibration did not have any effects on the result based on T-test and entropy distances. However, comparing the extracted feature values in ground truth data measured in calibrated and un-calibrated orthomosaics states partly different values in the both study areas (Figure 9).

Preprints (www.preprints.org) | NOT PEER-REVIEWED | Posted: 13 February 2019 doi:10.20944/preprints201902.0111.v1

Peer-reviewed version available at European Journal of Remote Sensing 2019, 52, 17-31; doi:10.1080/22797254.2019.1642143

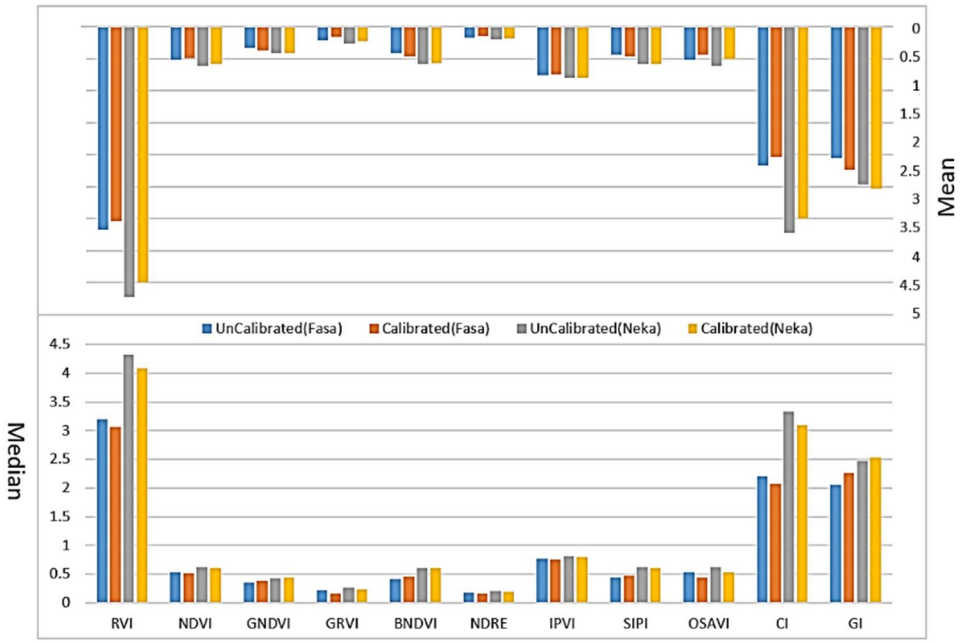

Figure 9: The feature values in ground truth data collected from calibrated and un-calibrated based orthomosaics

3.5. Classification

Three main classes were determined as un-healthy trees, healthy trees and non-trees at the study sites. Using the red and near infra-red spectral bands, the non-tree class was easily separated exactly from the trees classes. However, the detection of healthy and un-healthy trees classes remained as the main challenge.

Five spectral bands, as well as some VI that have high discrimination between healthy and un-healthy classes based on T-test and entropy criteria (Figure 8) and low correlation together (Table 7) were used in a random forest classifier consisting of 100 decision trees.

Table 7. Vegetation indices correlations at the Fasa study site

	RVI	NDVI	GNDVI	GRVI	BNDVI	NDRE	IPVI	SIPI	OSAVI	CI	DVI	GI
RVI	1.0000	0.9747	0.6263	0.2655	0.5205	0.5056	0.9747	0.7575	0.9450	1.0000	0.3300	0.6213
NDVI		1.0000	0.6410	0.2651	0.5340	0.5147	1.0000	0.7743	0.9653	0.9747	0.3277	0.6133
GNDVI			1.0000	-0.5672	0.6327	0.7706	0.6410	0.7139	0.5748	0.6263	0.0137	0.9757
GRVI				1.0000	-0.2257	-0.4167	0.2651	-0.0685	0.3106	0.2655	0.3321	-0.5760
BNDVI					1.0000	0.4172	0.5340	0.9468	0.5358	0.5205	0.2240	0.6276
NDRE						1.0000	0.5147	0.5069	0.3437	0.5056	-0.4210	0.7549
IPVI							1.0000	0.7743	0.9653	0.9747	0.3277	0.6133
SIPI								1.0000	0.7622	0.7575	0.2892	0.6999
OSAVI									1.0000	0.9450	0.5552	0.5536
CI										1.0000	0.3300	0.6213
DVI											1.0000	0.0227
GI												1.0000

From Table 7, it is obvious that there were higher correlations between RVI, NDVI, IPVI, OSAVI, and CI, between BNDVI and SIPI, and between GNDVI and GI; similar results were obtained for the other study site.

At the Fasa study site, five spectral bands as well as DVI, NDRE, NDVI, and GNDVI vegetation indices were used in the classification process of un-calibrated and calibrated orthomosaics. Figure 10 shows the generated map of the healthy and Greening infected trees and non-trees. There was insignificant difference in the classification maps (Figure 10). Small differences in results were observable, although were not significant.

Preprints (www.preprints.org) | NOT PEER-REVIEWED | Posted: 13 February 2019 doi:10.20944/preprints201902.0111.v1

Peer-reviewed version available at European Journal of Remote Sensing 2019, 52, 17-31; doi:10.1080/22797254.2019.1642143

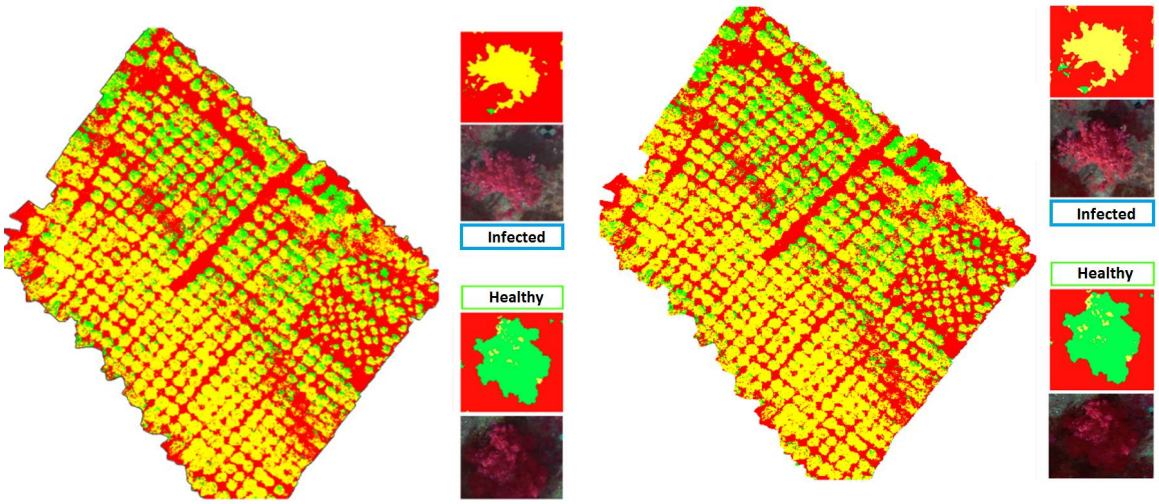

Figure 10. The classification map of healthy trees (green), Greening infected trees (yellow) and non-trees (red) based on the un-calibrated (Left) and calibrated (Right) orthomosaics at the Fasa study site

The overall accuracy and kappa values for both un-calibrated and calibrated based orthomosaic classifications were 96.6% and 0.94, respectively. The confusion matrix and estimated user's and producer's accuracy measures are also presented in Table 8 (un-calibrated orthomosaic) and Table 9 (calibrated orthomosaic).

Table 8. The confusion matrix and estimated user's and producer's accuracy of un-calibrated orthomosaic at the Fasa site

Confusion Matrix				
		Classified Data		
		Disease	Healthy	Non-tree
Test Data	Disease	93.1%	7.8%	0.1%
	Healthy	6.9%	92.2%	0%
	Non-tree	0%	0%	99.9%
User's and Producer 's Accuracy				
Class/Accuracy		User (%)	Producer (%)	
Un-healthy		93.1	96.6	
Healthy		92.2	84.6	
Non-tree		99.99	100	

Table 9. The confusion matrix and estimated user's and producer's accuracy of calibrated orthomosaics at the Fasa site

Confusion Matrix				
		Classified Data		
		Disease	Healthy	Non-tree
Test Data	Disease	92.8%	6.9%	0.1%
	Healthy	7.1%	93.1%	0%
	Non-tree	0%	0%	99.9%
User's and Producer 's Accuracy				
Class/Accuracy		User (%)	Producer (%)	
Un-healthy		93.1	96.6	
Healthy		92.2	84.6	

Preprints (www.preprints.org) | NOT PEER-REVIEWED | Posted: 13 February 2019 doi:10.20944/preprints201902.0111.v1

Peer-reviewed version available at European Journal of Remote Sensing 2019, 52, 17-31; doi:10.1080/22797254.2019.1642143

Non-tree	99.99	100

At the Neka study site, classification of the un-calibrated and calibrated orthomosaics is performed using five spectral bands as well as NDRE, BNDVI, GNDVI, DVI, and NDVI vegetation indices.

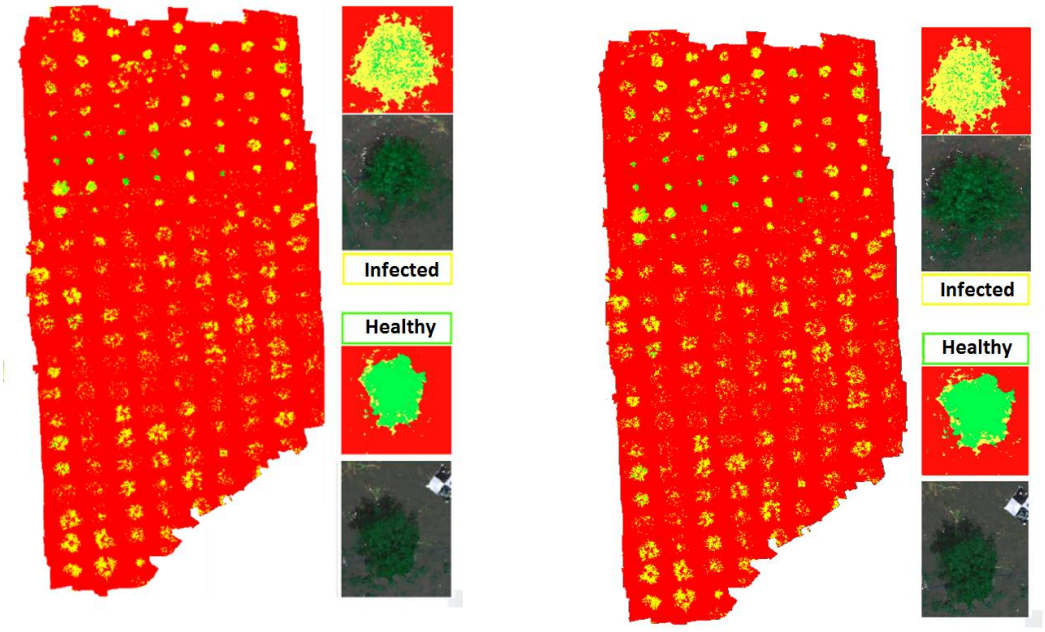

Figure 11 the classification result of healthy, Leaf Peach Curve infected and non-trees at the Neka study site. As in the Fasa data set, no significant difference in the classification map is observable (

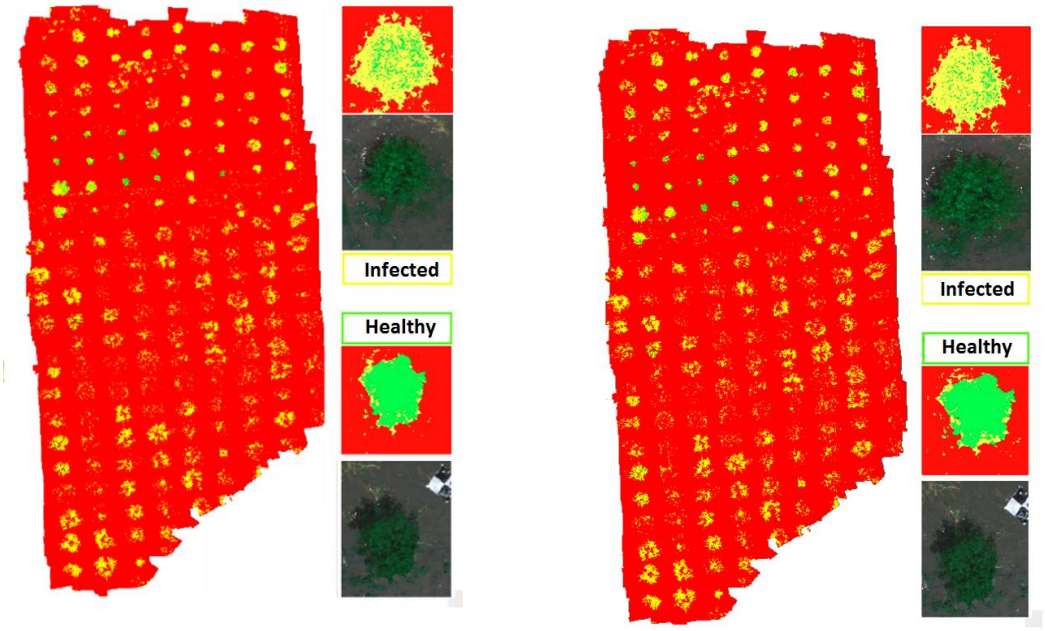

Figure 11).

Peer-reviewed version available at European Journal of Remote Sensing 2019, 52, 17-31; doi:10.1080/22797254.2019.1642143

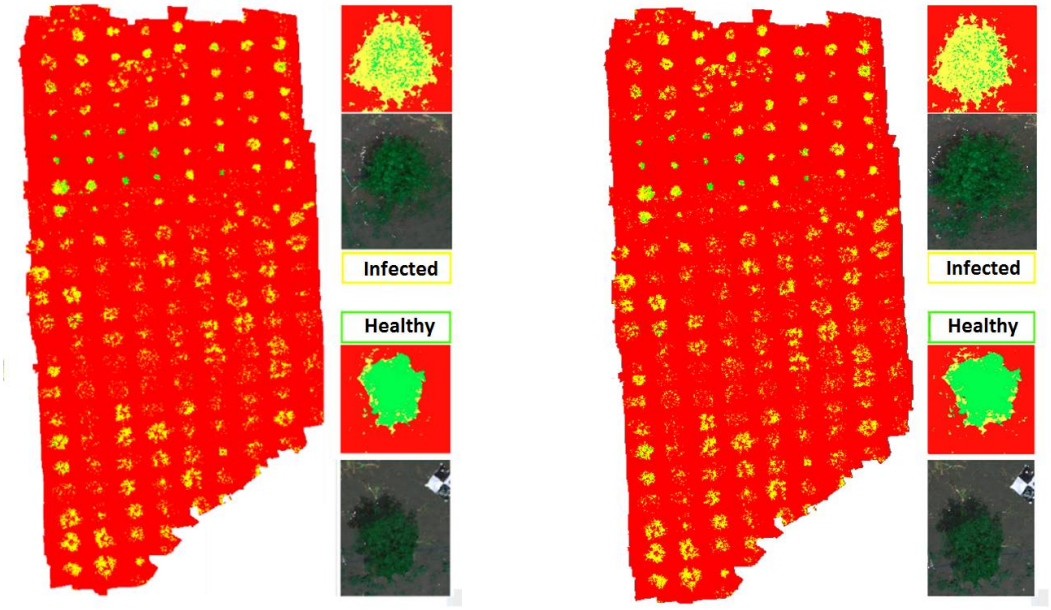

Figure 11. The classification map of healthy trees (green), leaf peach curve infected trees (yellow) and non-trees (red) or the un-calibrated (left) and calibrated (right) orthomosaics at the Neka study site

Achieved overall accuracy and kappa values for both the un-calibrated and calibrated orthomosaic classifications were 96.1% and 0.92, respectively. The confusion matrix and estimated user's and producer's accuracy measures are also computed and presented in Table 10 and **Table 11**, respectively.

Table 10. The confusion matrix and estimated user's and producer's accuracy of un-calibrated orthomosaic at the Neka site

Confusion Matrix				
		Classified Data		
		Disease	Healthy	Non-tree
Test Data	Disease	87.6%	9.7%	0.1%
	Healthy	11.9%	90.3%	0.1%
	Non-tree	0.5%	0%	99.8%
User's and Producer 's Accuracy				
Class/Accuracy		User (%)	Producer (%)	
Disease		87.6	86.0	
Healthy		90.3	91.2	
Non-tree		99.8	99.9	

Table 11. The confusion matrix and estimated user's and producer's accuracy of calibrated orthomosaics at the Neka site

Peer-reviewed version available at European Journal of Remote Sensing 2019, 52, 17-31; doi:10.1080/22797254.2019.1642143

Confusion Matrix				
		Classified Data		
		Disease	Healthy	Non-tree
Test Data	Disease	86.7%	9.1%	0.1%
	Healthy	12.6%	90.8%	0.1%
	Non-tree	0.7%	0.1%	99.8%
User's and Producer 's Accuracy				
Class/Accuracy		User (%)	Producer (%)	
Disease		86.7	86.8	
Healthy		90.8	90.7	
Non-tree		99.8	99.8	

Inspecting results, it can be concluded that radiometric calibration of images has minor effect on the classification accuracy. In the both statuses, almost the same precision was achieved and the confusion matrix components were not significantly different.

4. Discussion

Radiometric calibration is mentioned as one of the main steps in UAV based plant disease detection, and measurements of reference targets are implemented in empirical line based methods by default.. To study the necessity of this process, in this paper, two study data with different environmental conditions and affected by different diseases were classified to generate a tree health state map. Therefore, different processing steps were analyzed and the focus was on the necessity of radiometric calibration.

The multi-lenses structure of the multispectral camera in low flight altitude missions created a considerable geometric displacement between the spectral bands (Figure 5) which is up to 25 pixels for our data. Here, the maximum height difference is about 10 meters. Ignoring this displacement will result in different spectral features for the same objects and will lead to unsuitable training data. Therefore, the band-to-band registration step is important in the application; here, even leaf size is important and will reduce the registration error up to an average RMSE of 0.4 Pixel. It has to be mentioned that in images with extremely small relief variances with respect to flight height or with not much small focusing elements, the registration process can be neglected. In this situation, the ortho generation process can reduce the displacement to an acceptable level.

Orthomusaic is generated based on aligned images with the accuracy of 0.85 pixel and generated dense point cloud. However, different illumination conditions in each capturing station heterogeneous final orthomosaics (Figure 6-Left) and corrupts training data like the previous step.

The next step to prepare the training data is radiometric calibration which is performed based on empirical lines and changes pixel values linearly in each band. Therefore, outputs of this step can change the spectral features values. As shown in Figure 9, variation in most of the VIs is small due to their relative nature.

The detection of the healthy and un-healthy tree classes was performed using a random forest classifier. For this purpose, feature space was produced, including five spectral bands and 12 vegetation indices. The best features were selected based on the separation criteria of the tree classes and the correlation between the features. The correlation ranges from 94.5% to 100% between RVI, NDVI, IPVI, OSAVI, and CI, is 94.7% between BNDVI and SIPI, and is 97.6% between GNDVI and GI (Table 7); thus, six features can be eliminated. Moreover, at the Fasa study site, the spectral bands DVI and NDRE made the highest separation whereas the spectral band BNDVI made the lowest separation between the healthy and un-healthy tree classes. On the other hand, at the Neka study site, NDRE and BNDVI made the highest separation while GRVI made the lowest separation between classes. Classification was carried out using the selected features, and results are presented in Table 8 to

Peer-reviewed version available at European Journal of Remote Sensing 2019, 52, 17-31; doi:10.1080/22797254.2019.1642143

Table 11. At the Fasa study site, citrus orchard with the greening disease, the overall accuracy and kappa values for both the un-calibrated and calibrated orthomosaic classifications were 96.6% and 0.94, respectively. Similarly, the experimental results at the Neka study site with PLC yielded the same conclusions. The overall accuracy and kappa values for both the un-calibrated and calibrated orthomosaic classifications were 96.1% and 0.92, respectively. However, because of the linear structure of radiometric calibration, separation of the healthy and un-healthy tree classes based on t-test and entropy criteria did not change using the most spectral features (Figure 8); consequently, there were insignificant differences in the classification results after radiometric calibration.

5. Conclusions

This study investigated the necessity of radiometric calibration in UAV based multispectral imagery for plant tree disease detection and classification applications. For this purpose, two study sites with different conditions of climate, date, tree species and disease types were selected and multispectral images were captured using a RedEdge camera mounted on a multirotor UAV.

Due to the multi-lens structure of the camera and the low flying altitude, the band-to-band miss-registration error was not negligible; therefore, in the first step, they were registered. Then, to generate seamless orthomosaics, the registered images were aligned and radiometric normalization was implemented.

Radiometric calibration effects on plant classification and disease detection were evaluated in two scenarios. First, discrimination of the healthy and un-healthy classes was compared using T-test and entropy distances considering ground truth data collected from calibrated and un-calibrated orthomosaics. The experimental results showed that the effects of radiometric calibration on separability criteria using most spectral features were insignificant . In the other scenario, the radiometric calibration effects on the accuracy of classification were investigated. For this purpose, the best features were selected based on the separation criteria of the tree classes and the correlation between the features. The random forest classifier was applied to detect diseased trees. Experimental results showed insignificant differences in the classification results after radiometric calibration. At the Fasa study site, the overall accuracy and kappa values for both un-calibrated and calibrated orthomosaic classifications were 96.6% and 0.94, respectively. On the other study site, the overall accuracy and kappa values for both un-calibrated and calibrated orthomosaic classifications were 96.1% and 0.92.

It should also be noted that the classifier was trained based on the training data collected from the original data; therefore, due to the small change in the vegetation indices values, future studies will focus on the efficiency of radiometric calibration on the classification based on spectral library training data.

References

1. Onisimo, M., D. Timothy, and G. Omer, *Remote Sensing of Crop Health for Food Security in Africa: Potentials and Constraints.* Remote Sensing Applications: Society and Environment, 2017.
2. Psirofonia, P., et al., *Use of Unmanned Aerial Vehicles for Agricultural Applications with Emphasis on Crop Protection: Three Novel Case-studies.* International Journal of Agricultural Science and Technology, 2017.
3. Sankaran, S., et al., *A review of advanced techniques for detecting plant diseases.* Computers and Electronics in Agriculture, 2010. **72**(1): p. 1-13.
4. Sankaran, S., et al., *Evaluation of visible-near infrared reflectance spectra of avocado leaves as a non-destructive sensing tool for detection of laurel wilt.* Plant disease, 2012. **96**(11): p. 1683-1689.

5. Lu, S., et al., *Comparing vegetation indices for remote chlorophyll measurement of white poplar and Chinese elm leaves with different adaxial and abaxial surfaces.* Journal of experimental botany, 2015. **66**(18): p. 5625-5637.
6. Haboudane, D., et al., *Hyperspectral vegetation indices and novel algorithms for predicting green LAI of crop canopies: Modeling and validation in the context of precision agriculture.* Remote sensing of environment, 2004. **90**(3): p. 337-352.
7. Hede, A.N.H., et al., *A new vegetation index for detecting vegetation anomalies due to mineral deposits with application to a tropical forest area.* Remote Sensing of Environment, 2015. **171**: p. 83-97.
8. Baret, F., *Estimation of Biophysical Variables from Satellite Observations*, in *Land Surface Remote Sensing in Agriculture and Forest*. 2017, Elsevier. p. 37-80.
9. Jia, L., et al. *Nitrogen status estimation of winter wheat by using an IKONOS satellite image in the north china plain*. in *International Conference on Computer and Computing Technologies in Agriculture*. 2011. Springer.
10. Li, H., et al., *'Extended spectral angle mapping (ESAM)'for citrus greening disease detection using airborne hyperspectral imaging.* Precision Agriculture, 2014. **15**(2): p. 162-183.
11. Hart, W. and V. Myers, *Infrared Aerial Color Photography for Detection of Populations of Brown Soft Scale in Citrus Groves 1 2 3.* Journal of Economic Entomology, 1968. **61**(3): p. 617-624.
12. Ye, X., et al., *Use of airborne multispectral imagery to discriminate and map weed infestations in a citrus orchard.* Weed biology and management, 2007. **7**(1): p. 23-30.
13. Huang, Y., Y. Lan, and W. Hoffmann, *Use of airborne multi-spectral imagery in pest management systems.* Agricultural Engineering International: CIGR Journal, 2008.
14. Katti, A.R., et al., *Band selection using forward feature selection algorithm for citrus Huanglongbing disease detection.* Journal of Biosystems Engineering, 2015. **40**(4): p. 417-427.
15. Sankaran, S., et al., *Visible-near infrared spectroscopy for detection of Huanglongbing in citrus orchards.* Computers and electronics in agriculture, 2011. **77**(2): p. 127-134.
16. Mishra, A., et al., *Evaluation of an active optical sensor for detection of Huanglongbing (HLB) disease.* biosystems engineering, 2011. **110**(3): p. 302-309.
17. Sankaran, S., et al., *Huanglongbing (citrus greening) detection using visible, near infrared and thermal imaging techniques.* Sensors, 2013. **13**(2): p. 2117-2130.
18. Ashourloo, D., M.R. Mobasheri, and A. Huete, *Developing two spectral disease indices for detection of wheat leaf rust (Pucciniatriticina).* Remote Sensing, 2014. **6**(6): p. 4723-4740.
19. Ranjitha, G., M. Srinivasan, and A. Rajesh, *Detection and estimation of damage caused by thrips Thrips tabaci (Lind) of cotton using hyperspectral radiometer.* Agrotechnology, 2014. **3**(1): p. 1-5.

20. Baranowski, P., et al., *Hyperspectral and thermal imaging of oilseed rape (Brassica napus) response to fungal species of the genus Alternaria.* PloS one, 2015. **10**(3): p. e0122913.
21. Franke, J. and G. Menz, *Multi-temporal wheat disease detection by multi-spectral remote sensing.* Precision Agriculture, 2007. **8**(3): p. 161-172.
22. Glaser, J., et al. *Development of a broad landscape monitoring system using hyperspectral imagery to detect pest infestation*. in *Hyperspectral Image and Signal Processing: Evolution in Remote Sensing, 2009. WHISPERS'09. First Workshop on*. 2009. IEEE.
23. Wójtowicz, M., A. Wójtowicz, and J. Piekarczyk, *Application of remote sensing methods in agriculture.* Communications in Biometry and Crop Science, 2016. **11**: p. 31-50.
24. Kelcey, J. and A. Lucieer. *Sensor correction and radiometric calibration of a 6-band multispectral imaging sensor for UAV remote sensing*. in *The 12th Congress of the International Society for Photogrammetry and Remote Sensing*. 2012.
25. Cevallos-Cevallos, J.M., et al., *GC–MS metabolomic differentiation of selected citrus varieties with different sensitivity to citrus huanglongbing.* Plant Physiology and Biochemistry, 2012. **53**: p. 69-76.
26. Moscatello, S., et al., *Peach leaf curl disease shifts sugar metabolism in severely infected leaves from source to sink.* Plant Physiology and Biochemistry, 2017. **112**: p. 9-18.
27. Pecknold, P.C., *Peach Leaf Curl.* 2015.
28. Agüera, F., F. Carvajal, and M. Pérez, *Measuring sunflower nitrogen status from an unmanned aerial vehicle-based system and an on the ground device.* Int. Arch. Photogramm. Remote Sens. Spat. Inf. Sci, 2011. **38**: p. 33-37.
29. Garcia-Ruiz, F., et al., *Comparison of two aerial imaging platforms for identification of Huanglongbing-infected citrus trees.* Computers and Electronics in Agriculture, 2013. **91**: p. 106-115.
30. Candiago, S., et al., *Evaluating multispectral images and vegetation indices for precision farming applications from UAV images.* Remote Sensing, 2015. **7**(4): p. 4026-4047.
31. De Castro, A., et al., *Optimum spectral and geometric parameters for early detection of laurel wilt disease in avocado.* Remote Sensing of Environment, 2015. **171**: p. 33-44.
32. Sarkar, S.K., et al. *Towards autonomous phytopathology: Outcomes and challenges of citrus greening disease detection through close-range remote sensing*. in *Robotics and Automation (ICRA), 2016 IEEE International Conference on*. 2016. IEEE.
33. Albetis, J., et al., *Detection of Flavescence dorée Grapevine Disease Using Unmanned Aerial Vehicle (UAV) Multispectral Imagery.* Remote Sensing, 2017. **9**(4): p. 308.
34. Berni, J.A., et al., *Thermal and narrowband multispectral remote sensing for vegetation monitoring from an unmanned aerial vehicle.* IEEE Transactions on Geoscience and Remote Sensing, 2009. **47**(3): p. 722-738.

35. Smith, G.M. and E.J. Milton, *The use of the empirical line method to calibrate remotely sensed data to reflectance.* International Journal of remote sensing, 1999. **20**(13): p. 2653-2662.
36. Miura, T. and A.R. Huete, *Performance of three reflectance calibration methods for airborne hyperspectral spectrometer data.* Sensors, 2009. **9**(2): p. 794-813.
37. Clemens, S.R., *Procedures for correcting digital camera imagery acquired by the AggieAir remote sensing platform.* 2012.
38. Honkavaara, E., et al., *Processing and assessment of spectrometric, stereoscopic imagery collected using a lightweight UAV spectral camera for precision agriculture.* Remote Sensing, 2013. **5**(10): p. 5006-5039.
39. Wijesingha, J., *Geometric quality assessment of multi-rotor unmanned aerial vehicle borne remote sensing products for precision agriculture.* Student thesis series INES, 2016.
40. Jhan, J.-P., J.-Y. Rau, and C.-Y. Huang, *Band-to-band registration and ortho-rectification of multilens/multispectral imagery: A case study of MiniMCA-12 acquired by a fixed-wing UAS.* ISPRS Journal of Photogrammetry and Remote Sensing, 2016. **114**: p. 66-77.
41. Lindeberg, T., *Scale invariant feature transform.* 2012.
42. Shi, J., J. Wang, and Y. Xu, *Object-based change detection using georeferenced UAV images.* Int. Arch. Photogramm. Remote Sens. Spat. Inf. Sci, 2011. **38**: p. 177-182.
43. Nissen, E., et al. *Rapid-Response or Repeat-Mode Topography from Aerial Structure from Motion*. in *AGU Fall Meeting Abstracts*. 2014.
44. Nesbit, P.R., *Uninhabited Aerial Vehicles and Structure from Motion: A fresh approach to photogrammetry*. 2014: California State University, Long Beach.
45. Gehrke, S. and B. Beshah, *RADIOMETRIC NORMALIZATION OF LARGE AIRBORNE IMAGE DATA SETS ACQUIRED BY DIFFERENT SENSOR TYPES.* International Archives of the Photogrammetry, Remote Sensing & Spatial Information Sciences, 2016. **41**.
46. Näsi, R., et al., *Using UAV-based photogrammetry and hyperspectral imaging for mapping bark beetle damage at tree-level.* Remote Sensing, 2015. **7**(11): p. 15467-15493.
47. Nevalainen, O., et al., *Individual tree detection and classification with UAV-based photogrammetric point clouds and hyperspectral imaging.* Remote Sensing, 2017. **9**(3): p. 185.
48. Joshi, P.C., *Performance evaluation of vegetation indices using remotely sensed data.* International Journal of Geomatics and Geosciences, 2011. **2**(1): p. 231.
49. Guyon, I. and A. Elisseeff, *An introduction to variable and feature selection.* Journal of machine learning research, 2003. **3**(Mar): p. 1157-1182.
50. Li, F., et al., *Estimating N status of winter wheat using a handheld spectrometer in the North China Plain.* Field Crops Research, 2008. **106**(1): p. 77-85.
51. Rouse Jr, J., *Monitoring the vernal advancement and retrogradation (green wave effect) of natural vegetation.* 1974.

52. Gitelson, A.A., Y.J. Kaufman, and M.N. Merzlyak, *Use of a green channel in remote sensing of global vegetation from EOS-MODIS.* Remote Sensing of Environment, 1996. **58**(3): p. 289-298.
53. Sripada, R.P., et al., *Aerial color infrared photography for determining early in-season nitrogen requirements in corn.* Agronomy Journal, 2006. **98**(4): p. 968-977.
54. Wang, F.-M., et al., *New vegetation index and its application in estimating leaf area index of rice.* Rice Science, 2007. **14**(3): p. 195-203.
55. Gitelson, A. and M.N. Merzlyak, *Spectral reflectance changes associated with autumn senescence of Aesculus hippocastanum L. and Acer platanoides L. leaves. Spectral features and relation to chlorophyll estimation.* Journal of Plant Physiology, 1994. **143**(3): p. 286-292.
56. Crippen, R.E., *Calculating the vegetation index faster.* Remote Sensing of Environment, 1990. **34**(1): p. 71-73.
57. Peñuelas, J., et al., *The reflectance at the 950–970 nm region as an indicator of plant water status.* International journal of remote sensing, 1993. **14**(10): p. 1887-1905.
58. Dash, J. and P.J. Curran, *The MERIS terrestrial chlorophyll index.* International Journal of Remote Sensing, 2004. **25**(23): p. 5403-5413.
59. Bausch, W. and R. Khosla, *QuickBird satellite versus ground-based multi-spectral data for estimating nitrogen status of irrigated maize.* Precision Agriculture, 2010. **11**(3): p. 274-290.
60. Jordan, C.F., *Derivation of leaf - area index from quality of light on the forest floor.* Ecology, 1969. **50**(4): p. 663-666.
61. Zarco-Tejada, P.J., et al., *Assessing vineyard condition with hyperspectral indices: Leaf and canopy reflectance simulation in a row-structured discontinuous canopy.* Remote Sensing of Environment, 2005. **99**(3): p. 271-287.
62. Breiman, L., *Random forests.* Machine learning, 2001. **45**(1): p. 5-32.
63. Joshi, A., et al. *A random forest approach to segmenting and classifying gestures*. in *Automatic Face and Gesture Recognition (FG), 2015 11th IEEE International Conference and Workshops on*. 2015. IEEE.
64. Feng, Q., J. Liu, and J. Gong, *UAV remote sensing for urban vegetation mapping using random forest and texture analysis.* Remote Sensing, 2015. **7**(1): p. 1074-1094.
65. Rodriguez-Galiano, V.F., et al., *An assessment of the effectiveness of a random forest classifier for land-cover classification.* ISPRS Journal of Photogrammetry and Remote Sensing, 2012. **67**: p. 93-104.
66. Rezaeian, M., R. Amirfattahi, and S. Sadri, *Semantic segmentation of aerial images using fusion of color and texture features.* 2014.